Electronic Supplementary Material (ESI) for Energy & Environmental Science

SUPPORTING INFORMATION FOR

Simulations of the irradiation and temperature dependence of the efficiency of tandem photoelectrochemical water-splitting systems

Sophia Haussener, Shu Hu, Chengxiang Xiang, Adam Z. Weber, and Nathan S. Lewis

Spatial and temporal variation in solar irradiation

Figure S1 depicts the spatial, hourly and seasonal variation in solar irradiation.

a) b)

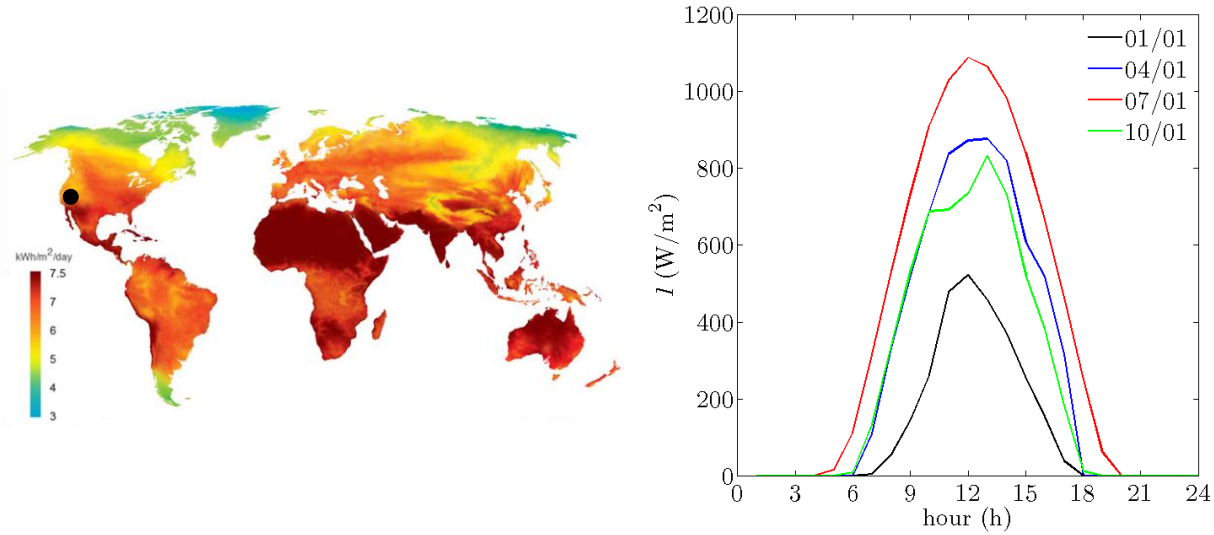

Figure S1. Annual mean of hourly solar irradiation (a), and hourly resolved irradiation for four characteristic seasonal days in Barstow, California (b).

Materials properties

Table S1 presents the properties of the materials chosen for the system as well as their temperature dependence between 300 K and 353 K. The increase in solution conductivity with temperature was approximated by

$$\kappa_{\mathrm{l}} = \kappa_{\mathrm{l},T=293\mathrm{K}}\left(1+\alpha\left[T-293\right]\right), \qquad \text{(S1)}$$

where $\kappa_{l,T=293K}$ and α were fitted to experimental data available for 1 M sulfuric acid [1]. The temperature dependence of the conductivity of a non-permeable polymeric membrane, i.e. Nafion, was given by

$$\kappa_{mem} = \kappa_{0,mem} \exp\left(-\frac{E_a}{RT}\right), \quad \text{(S2)}$$

where E_a represents the activation energy [2]. The decrease in the equilibrium potential for the one-step water-electrolysis reaction with increasing temperature is given by

$$U = U_\theta - T \cdot \alpha_3, \quad \text{(S3)}$$

where U_θ is the equilibrium potential assuming a hydrogen reference electrode, and α_3 is given by the temperature-dependence of the Gibbs free energy (ΔG=-nFU).The electrochemical reactions were described by Butler-Volmer expressions,

$$i_{R,OER/HER} = i_{0,OER/HER}\left[\left(\frac{c_{red}}{c_{red,0}}\right)^{\gamma_{red}} \exp\left(\frac{\alpha_{a,OER/HER} F\eta_{op}}{RT}\right) - \left(\frac{c_{ox}}{c_{ox_0}}\right)^{\gamma_{ox}} \exp\left(\frac{-\alpha_{c,OER/HER} F\eta_{op}}{RT}\right)\right], \quad \text{(S4)}$$

with

$$i_{0,OER/HER} = i_{0,OER/HER,T_{ref}} \exp\left(-\frac{E_a}{RT}\right). \quad \text{(S5)}$$

The kinetic parameters used in the study are for state-of-the-art catalysts, i.e. Pt-based electrodes for the HER reaction and RuO_2-based electrodes for the OER reaction. For the HER, transfer coefficients between 1 and 2 have been reported [3], and values of $\alpha_{a,HER} = \alpha_{c,HER} = 1$ were assumed. For the OER, $\alpha_{a,HER} = 1.7$ and $\alpha_{c,HER} = 0.1$ were used, which is consistent with the reported 35 mV per decade Tafel slope [4] as well as an assumed negligible back reaction at the potential of interest. The temperature dependences were extracted from various experimental studies [5-8].

The temperature-dependent conductivity of a transparent conducting oxide (TCO) layer was given by

$$\sigma_{\mathrm{TCO}} = \frac{A_0}{R_{\mathrm{s},0} t} \exp\left(-\frac{\Delta E}{kT}\right), \tag{S6}$$

where R_s is the sheet resistance of the TCO material of thickness t, and ΔE is the activation energy in eV [9]. The temperature dependence of the band gap was described using the Varshi model[10-12],

$$E_g = E_{g,0} - \frac{\alpha_2 T^2}{T + \beta} \tag{S7}$$

with the constants α_2 and β fitted to experimental data for Si and GaAs [12].

Table S1. Parameters used for the various materials and components in the system, as a function of temperature.

Parameter	Value	Param.	Value	Param.	Value	Ref.
$i_{0,\mathrm{OER},T\mathrm{ref}}$	4.62 A cm^{-2}	$E_{a,\mathrm{OER}}$	48.6 kJ mol^{-1}	-	-	5, 6, 13
$i_{0,\mathrm{HER},T\mathrm{ref}}$	142.02 A cm^{-2}	$E_{a,\mathrm{HER}}$	28.9 kJ mol^{-1}	-	-	7, 8
$\kappa_{0,\mathrm{mem}}$	22.73 S m^{-1}	$E_{a,\mathrm{mem}}$	2 kJ mol^{-1}	-	-	2, 14
$\kappa_{l,T=293\mathrm{K}}$	40 S m^{-1}	α	0.019 K^{-1}	-	-	1
$R_{s,0}$	10 Ω/□	A_0	3.695	ΔE	0.033 eV	9
$E_{g,0,\mathrm{Si}}$	1.1557 eV	$\alpha_{2,\mathrm{Si}}$	7.021·10^{-4} eV K^{-1}	β_{Si}	1108 K	10, 12
$E_{g,0,\mathrm{GaAs}}$	1.5216 eV	$\alpha_{2,\mathrm{GaAs}}$	8.871·10^{-4} eV K^{-1}	β_{GaAs}	572 K	10, 12
A_{H2}	-48.1611	B_{H2}	55.2845	C_{H2}	16.8893	15
A_{O2}	-66.7354	B_{O2}	87.4755	C_{O2}	24.4526	15

Table S1 also presents the set of parameters used in this study. The supporting information shows detailed current-voltage behavior and characteristics (i_{sc}, V_{oc}, FF) of dual-

absorber tandem cells for hourly, seasonal, and local variations in the solar irradiation and for various isothermal system temperatures.

The temperature-dependence of the saturation concentrations of H_2(g) and O_2(g) were given by

$$c_{\mathrm{sat},k} = \exp\left(A_k + B_k / (T/100\mathrm{K}) + C_k \ln(T/100\mathrm{K})\right) / M_{\mathrm{H_2O}} \cdot 1000, \qquad \text{(S8)}$$

in the units mol/m^3.

Semiconductor performance and characterization

Figure S2 depicts the change in current-voltage characteristics of a dual-absorber tandem cell (made of 1.7/1.1 eV bandgap materials) during a typical summer day at Barstow.

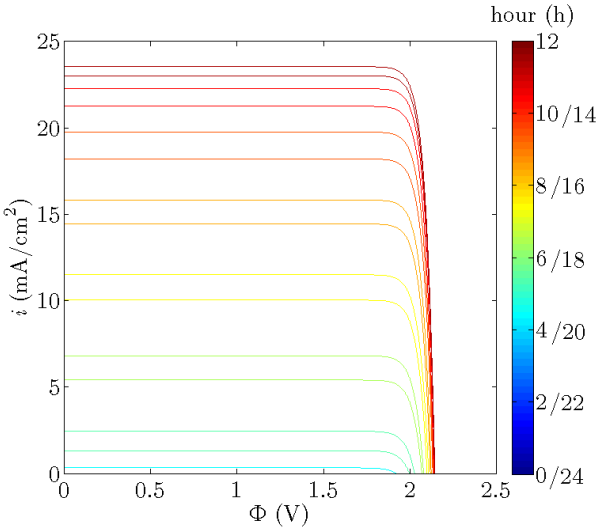

Figure S2. Current vs. voltage performance and its variation during the day of a dual-absorber tandem cell composed of 1.7/1.1 eV bandgap materials for a typical July day.

Figure S3 depicts the short-circuit current density, open-circuit voltage, and fill factor (FF) of two characteristic types of dual-absorber tandem cells, i.e. (*i*) a current-matched cell composed of 1.7/1.1 eV band gap materials (i.e. GaAsP/Si), and (*ii*) a non-current matched

cell composed of 1.43/1.1 eV band gap materials (i.e. GaAs/Si). The short-circuit current density is proportional to the solar irradiation.

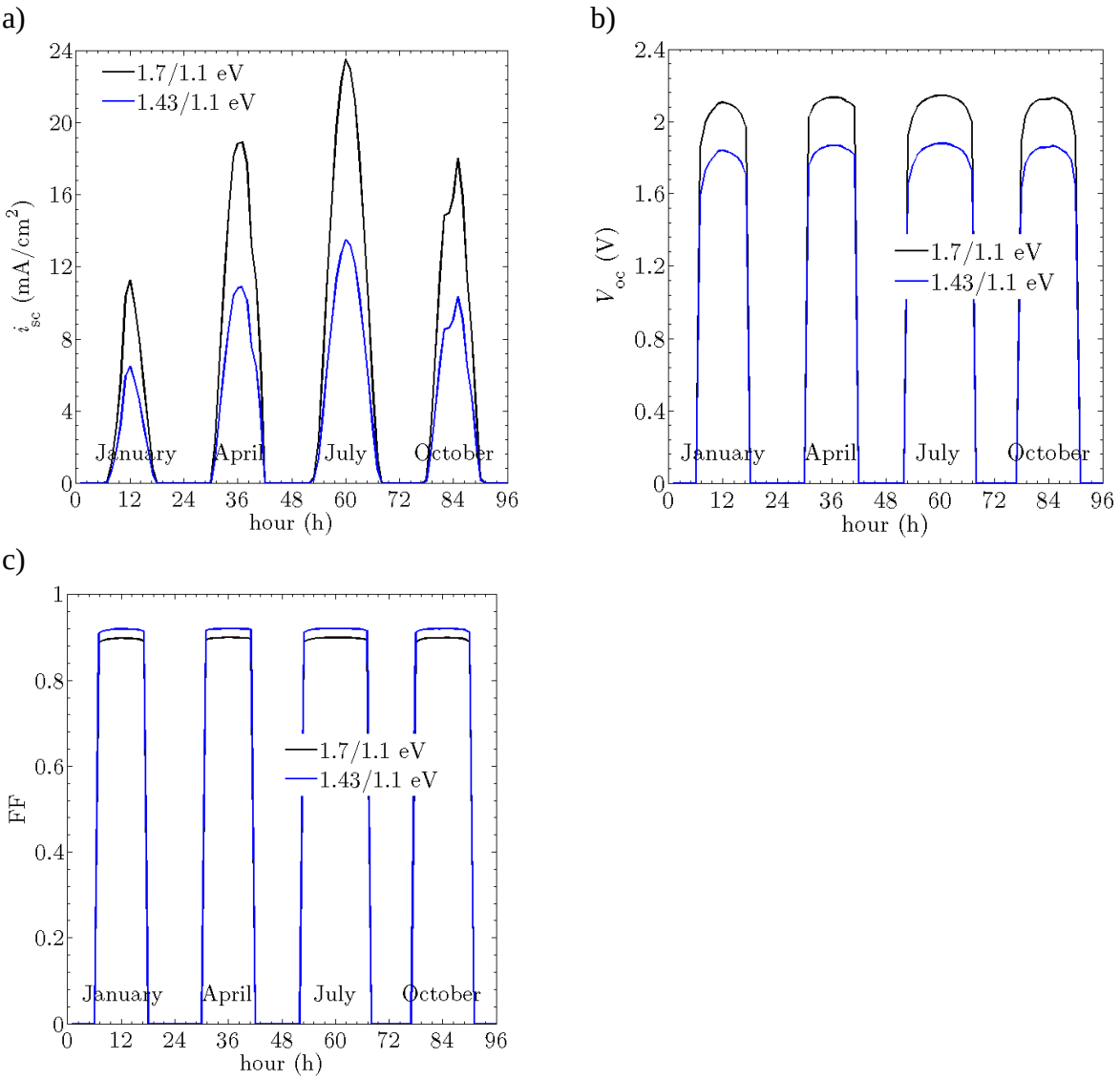

Figure S3. Variation in short-circuit current density (a), open-circuit potential difference (b), and form factor (c), of the current matching (1.7/1.1 eV) and non-current matching (1.43/1.1 eV) dual-cells during four typical days in winter, spring, summer, and fall.

Figure S4 depicts the short-circuit current density, open-circuit voltage, and fill factor (FF) of two dual-absorber tandem cells, for variations in the isothermal system temperature (between 300 K and 353 K). The short-circuit current density decreases for a dual-absorber tandem cell

because the current-matching band gap combination evolves into a less favorable current combination (a non-current matching) as the temperature is changed. The results are in accord with reported data [12].

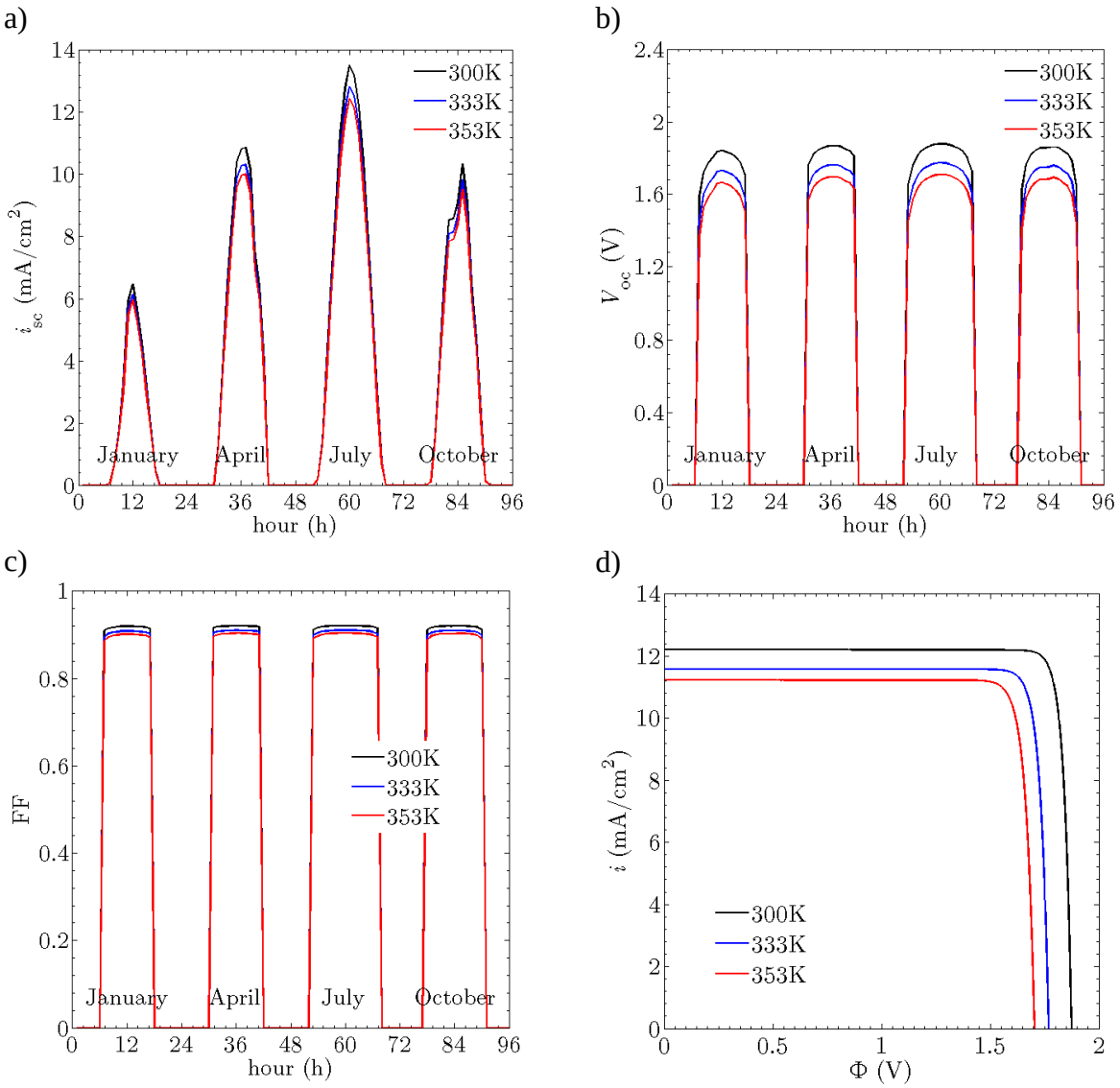

Figure S4. Temperature-dependent short-circuit current density (a), open-circuit voltage (b), fill factor (c), and i-V-performance for I=1kWm^{-2}, for the dual cell composed of 1.43/1.1 eV band gaps (at room temperature).

An artificial series resistance within the semiconductor model was used to more accurately account for non-idealities. Figure S5 depicts the current density vs. voltage performance of a dual-absorber tandem cell.

Figure S6 depicts the changes in short-circuit current density, open-circuit voltage, and fill factor for various combinations of band gaps at 1kW/m^2, 1.5 AM solar irradiation.

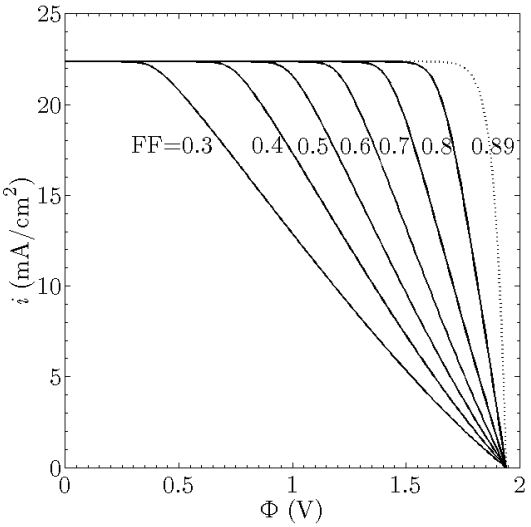

Figure S5. Current density vs. voltage performance and its change with increasing series resistance, i.e. decreasing fill factor, for a 1.6/1.0 eV band gap dual-absorber tandem cell for 1 sun and 1.5 AM solar irradiation. The dotted line depicts the detailed balance limit.

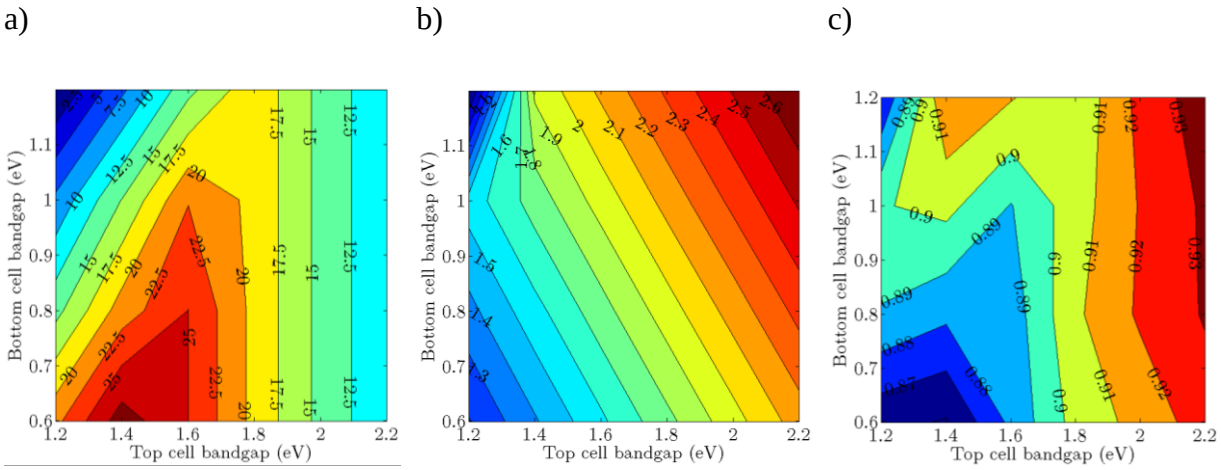

Figure S6. (a) Short-circuit current density (mA/cm^2), (b) open-circuit voltage (V), and (c) fill factor for various combinations of top and bottom bandgap energies at 1 kW/m^2, 1.5 AM solar irradiation.

Realistic dual absorbed tandem cell

The performance of a realistic dual absorber tandem cell composed of currently available Si and GaAs cells has also been predicted via the measured performance of individual single cells, as given in Table S2.

Table S2. Measured short-current density, open-circuit voltage, fill factor, and temperature coefficients of commercial GaAs (Alta devices[*]) or Si (Schott [†,16]) solar cells.

	GaAs cell	Si cell
$i_{sc,0}$	24.39 mA cm^{-2}	42.7 mA cm^{-2}
$V_{oc,0}$	1.09 V	0.706 V
FF	0.842	0.828
α_{abs}	0.084 % K^{-1}	0.03 % K^{-1}
γ_{abs} or β_{abs}	0.187 % K^{-1}	2 mV K^{-1}

The intensity dependence and temperature dependence of the performance can be approximated as:

$$i_{sc} = i_{sc,0}\left(1+\alpha_{abs}\left[T-298\right]\right)\cdot\frac{I}{I_0}, \quad \text{(S9)}$$

$$V_{sc} = V_{sc,0}\left(1+\gamma_{abs}\left[T-298\right]\right), \quad \text{(S10)}$$

$$V_{oc} = V_{oc,0}-\beta_{abs}\left(T-298\right), \quad \text{(S11)}$$

with the measured temperature coefficients α_{abs}, γ_{abs}, and β_{abs}. The performance of the tandem configuration was calculated by using the Si and GaAs cells in series, with the irradiation of the bottom cell (Si) reduced by the fraction of light absorbed by the top cell (GaAs), as given by its temperature-dependent band gap energy calculated using equation (S7).

[*] www.altadevices.com/pdfs/single_cell.pdf
[†] http://www.schott.com/photovoltaic/english/download/schott_perform_mono_255-270_3bb_new_frame_data_sheet_en_0312.pdf

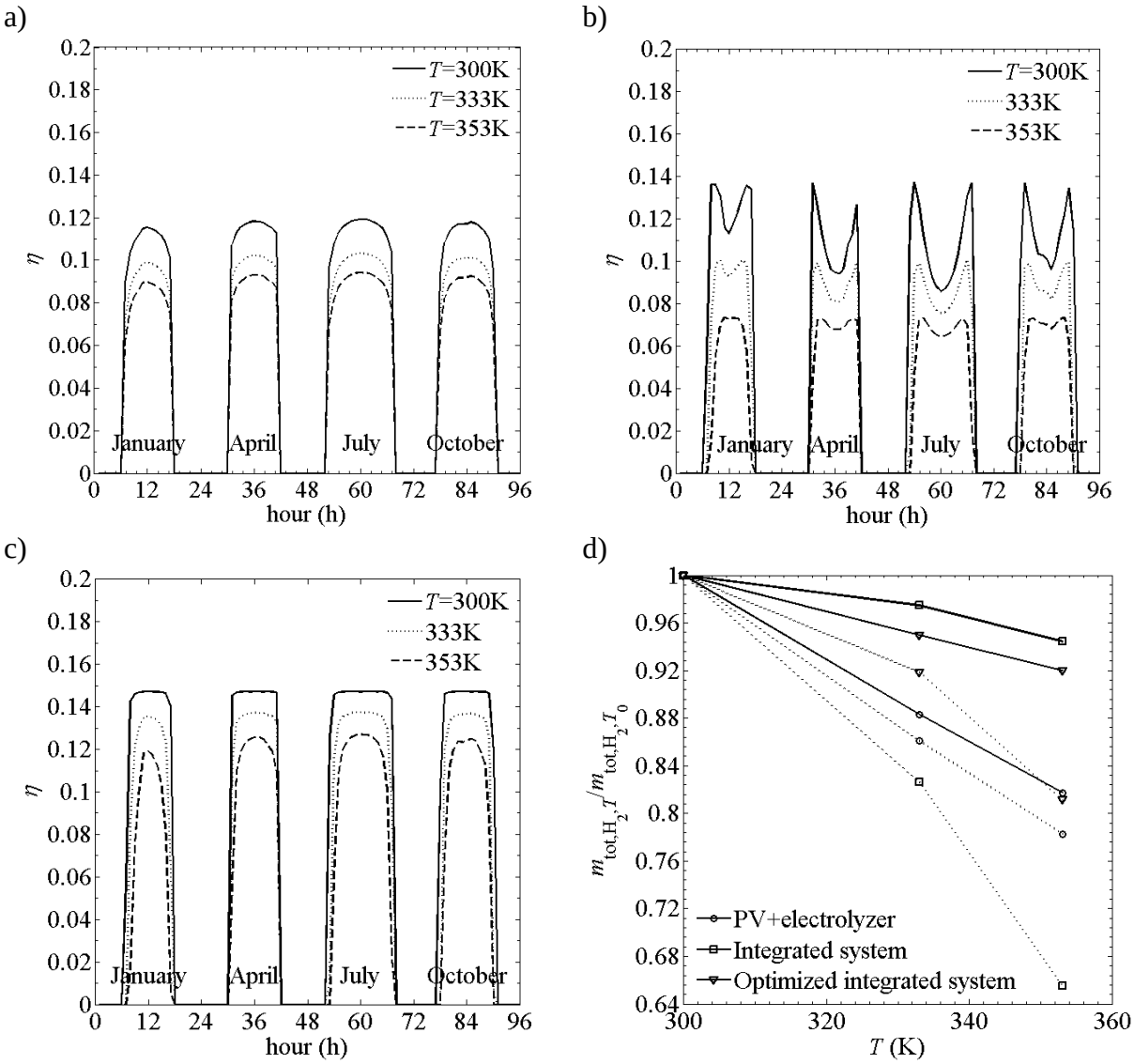

Figure S7. (a) η of a conventional stand-alone PV system with a Si/GaAs dual absorber tandem structure based on the measured individual cell performance, with the tandem cell electrically connected to a stand-alone electrolyzer, for four typical seasonal days at three isothermal conditions (T = 300, 333, 353 K), and (b,c) η of a PEC device with a Si/GaAs dual absorber tandem-cell based on measured individual cell performance for four typical seasonal days at three isothermal conditions (T = 300, 333, 353 K) for design B with η_{pc} = 1, (b) l_{el} = 50 mm, and t_e = 1 mm, and (c) l_{el} = 10 mm, and t_e = 10 mm, and (d) the normalized annually integrated fuel production for the conventional system and for the integrated system with m_{tot,H_2,T_0} = 6.6, 5.9, and 8.3 kg m^{-2} year^{-1} for the PV+electrolyzer, the integrated system, and the optimized integrated system, respectively, for detailed balance limit (solid line) and the realistic case (dotted line).

The resulting performance of the integrated system and a stand-alone tandem PV plus stand-alone electrolyzer system (electrolyzer efficiency of 75% and a DC-DC-converter efficiency of 85%) using Si/GaAs-based dual absorber tandem-cell based on measured single cell performance are depicted in Figure S7.

As observed for systems that were assumed to operate in the Shockley-Quiesser limit, unlike the integrated solar fuels generator system, the realistic stand-alone PV plus stand-alone electrolyzer system displayed its highest η during mid-day and its highest $\overline{\eta}_{d}$ at mid-year. Increases in the temperature from 300 K to 353 K of the light absorber components of the discrete system decreased $\overline{\eta}_{a}$ of the stand-alone system combination from 11.2% to 8.7%, with a slight increase in σ_{a} (from 0.24% to 0.27%). The integrated system for design B with $\eta_{pc} = 1$, $l_{el} = 50$ mm, and $t_{e} = 1$ mm, showed $\overline{\eta}_{a}$ = 11.3% and 6.4% for T = 300 K and 353 K, respectively, with slight increase in σ_{a} (from 0.02% to 0.03%). Changing the dimensions of the system to $l_{el} = 10$ mm, and $t_{e} = 10$ mm resulted in an increase in $\overline{\eta}_{a}$ to values of 14.3% and 10.6% for T = 300 K and 353 K, respectively, with decrease in σ_{a} (from 0.34% to 0.28%). Figure S7d shows the normalized, annually integrated fuel production for the stand-alone PV and stand-alone electrolyzer combination, as well as for two cases of the integrated solar fuels generator system: *i*) with $l_{el} = 50$ mm and $t_{e} = 1$ mm and a large total overpotential, and *ii*) the optimized case for l_{el} = 10 mm and t_{e} = 10 mm with a small, non-limiting total overpotential. The mass of H_2 produced annually, m_{tot,H_2,T_0}, was 6.6, 5.9, and 8.3 kg m^{-2} $year^{-1}$ for the stand-alone PV and stand-alone electrolyzer combination, the integrated system, and the optimized integrated system, respectively at an absorber operating temperature of 300 K in all cases.

Integrated vs. stand-alone PV plus stand-alone electrolyzer system

η, $\overline{\eta}_d$, $\overline{\eta}_a$, σ_a, and the yearly amount of fuel produced by an integrated solar fuels generator system were compared to the behavior of a system instead comprised of a conventional photovoltaic (PV) module-based stand-alone system coupled electrically to a stand-alone electrolysis unit. The efficiency of the system comprised of the discrete components can be described by equation (11). An electrolyzer efficiency of 75% and a DC-DC-converter efficiency of 85% were used in the calculations.

Figure S8 shows the performance of the stand-alone PV system in combination with the stand-alone electrolyzer system. The dual absorber tandem-cell of the PV system was taken to consist of 1.0/1.6 eV band-gaps at all temperatures, which showed to lead to the best tandem-cell PV performance. Unlike the integrated solar fuels generator system, the stand-alone PV plus stand-alone electrolyzer system displayed its highest η during mid-day and its highest $\overline{\eta}_d$ at mid-year. Increases in the temperature, from 300 K to 353 K, of the light absorber components of the discrete system decreased $\overline{\eta}_a$ of the stand-alone system combination from 24.2% to 21.9%, with a slight increase in σ_a (from 0.97% to 1.13%). The band-gap of the light absorber usually decreases by 0.002 to 0.006 eV K^{-1} [12] and therefore this straight-forward comparison neglects the penalty due to reduced current matching, i.e. lower i_{sc}, of such a dual absorber tandem-cell at higher temperatures.

a)

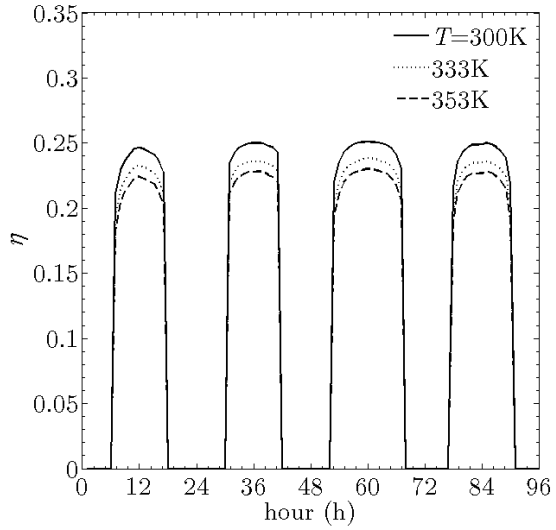

b)

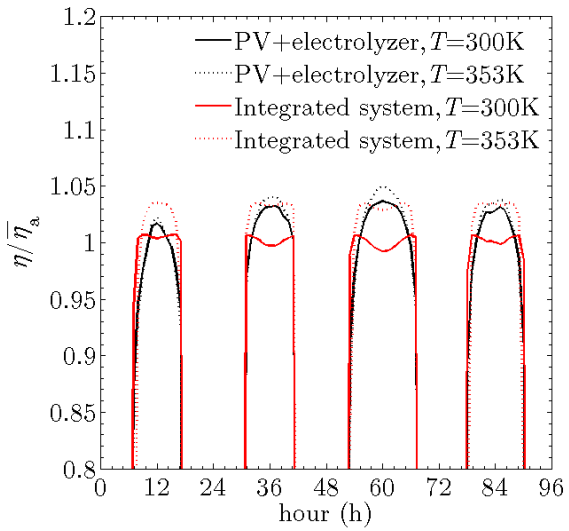

c)

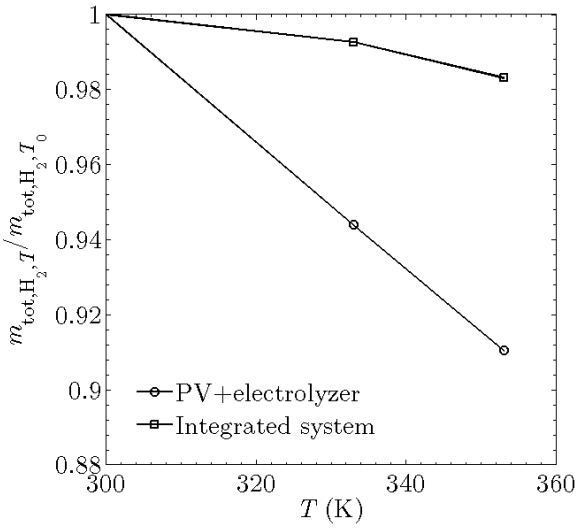

Figure S8. (a) η of a conventional stand-alone PV system with its optimal band-gap combination for the dual absorber tandem-cell (1.0/1.6 eV at all temperatures), electrically connected to a stand-alone electrolyzer, for four typical seasonal days at three isothermal conditions (T = 300, 333, 353 K), and (b) the instantaneous efficiency normalized by $\overline{\eta}_a$ for the stand-alone PV plus stand-alone electrolyzer system compared to the instantaneous efficiency of an integrated solar fuels generator system with l_{el} = 10 mm, t_e = 10 mm, and η_{pc} = 1, at its optimal band-gap combination (0.8/1.6 eV at all temperatures) and (c) the normalized annually integrated fuel production for the conventional system and for the integrated system with m_{tot,H_2,T_0} = 14.0, and 17.4 kg m^{-2} year^{-1} for the PV+electrolyze and integrated system, respectively.

References

1 H. E. Darling, *Journal of Chemical & Engineering Data*, 1964, **9**, 421–426.

2 Y. Sone, P. Ekdunge and D. Simonsson, *Journal of The Electrochemical Society*, 1996, **143**, 1254–1259.

3 J. O. M. Bockris, I. A. Ammar and A. K. M. S. Huq, *The Journal of Physical Chemistry*, 1957, **61**, 879–886.

4 G. Lodi, E. Sivieri, A. Battisti and S. Trasatti, *Journal of Applied Electrochemistry*, 1978, **8**, 135–143.

5 K. Kinoshita, *Electrochemical Oxygen Technology*, John Wiley and Sons, Inc.,, 1992.

6 L. Kriksunov, L. Bunakova, S. Zabusova and L. Krishtalik, *Electrochimica Acta*, 1994, **39**, 137 – 142.

7 N. M. Markovic, B. N. Grgur and P. N. Ross, *The Journal of Physical Chemistry B*, 1997, **101**, 5405–5413.

8 W. Sheng, H. A. Gasteiger and Y. Shao-Horn, *Journal of The Electrochemical Society*, 2010, **157**, B1529–B1536.

9 J. George and C. Menon, *Surface and Coatings Technology*, 2000, **132**, 45 – 48.

10 Y. Varshni, *Physica*, 1967, **34**, 149 – 154.

11 R. Pässler, *physica status solidi (b)*, 2003, **236**, 710–728.

12 P. Singh and N. Ravindra, *Solar Energy Materials and Solar Cells*, 2012, **101**, 36 – 45.

13 A. Damjanovic, A. Dey and J. O. Bockris, *Journal of The Electrochemical Society*, 1966, **113**, 739–746.

14 H. Ito, T. Maeda, A. Nakano and H. Takenaka, *International Journal of Hydrogen Energy*, 2011, **36**, 10527 – 10540.

15 W. Haynes, *CRC Handbook of Chemistry and Physics*, Taylor & Francis, 2011.

16 M. A. Green, K. Emery, Y. Hishikawa, W. Warta and E. D. Dunlop, *Progress in Photovoltaics: Research and Applications*, 2013, **21**, 1–11.